Size-resolved chemical composition, effective density, and optical properties of biomass burning particles

Jinghao Zhai[1], Xiaohui Lu[1], Ling Li[1], Qi Zhang[1,2], Ci Zhang[1], Hong Chen[1], Xin Yang[1]*, Jianmin Chen[1]

[1]*Shanghai Key Laboratory of Atmospheric Particle Pollution and Prevention, Department of Environmental Science and Engineering, Fudan University, Shanghai 200433, China*

[2]*Department of Environmental Toxicology, University of California, Davis, California 95616, United States*

Correspondence to: Xin Yang (yangxin@fudan.edu.cn)

Abstract. Biomass burning aerosol has important impact on the global radiative budget. A better understanding of the correlations between the mixing states of biomass burning particles and their optical properties is the goal of a number of current studies. In this work, effective density, chemical composition, and optical properties of rice straw burning particles in the size range of 50-400 nm were measured using a suite of online methods. We found that the major components of rice straw burning particles included black carbon (BC), organic carbon (OC) and potassium salts, but the mixing states of particles were strongly size-dependent. Particles of 50 nm had the smallest effective density (1.16 g/cm^3), due to a relatively large proportion of aggregate BC. The average effective densities of 100-400 nm particles ranged from 1.35-1.51 g/cm^3 with OC and inorganic salts as dominant components. Both density distribution and single-particle mass spectrometry showed more complex mixing states in larger particles. Upon heating, the separation of the effective density distribution modes testified the external mixing state of less volatile BC or soot and potassium salts. Size-resolved optical properties of biomass burning particles were investigated at two wavelengths (λ=450 & 530 nm). The single scattering albedo (SSA) showed the lowest value for 50 nm particles (0.741±0.007 & 0.889±0.006) because of the larger proportion of BC content. Brown carbon played an important role for the SSA of 100-400 nm particles. The Ångström absorption exponent (AAE) values for all particles were above 1.6, indicating the significant presence of brown carbon in all sizes. Concurrent measurements in our work provide a basis for discussing the physicochemical properties of biomass burning aerosol and its effects on global climate and atmospheric environment.

1 Introduction

Biomass burning is a significant source of trace gases and aerosol particles (Andreae and Merlet, 2001). Biomass burning particles affect climate by both absorbing and scattering solar radiation (Chand et al., 2009) and serve as cloud condensation nuclei which would modify cloud microphysical properties (Petters et al., 2009). In addition, biomass burning particles have considerable impacts on air quality, regional visibility, and human health (Naeher et al., 2007; Park et al., 2006). Global annual emissions of black carbon (BC) and organic carbon (OC) aerosols are estimated to be ~8 and 33.9

Tg yr^{-1} while open burning contributes approximately 42% for BC and 74% for OC (Bond et al., 2004). Along with rapid economic development and increase in agricultural activities, emissions from agricultural residue combustion in China have drawn extensive attention. The total amount of straws from open burning in China is estimated to be ~140 Tg yr^{-1} (Cao et al., 2008).

Mixing state, composition, and morphology of particles can influence their radiative properties. BC, which is predominantly produced from the combustion related sources, absorbs solar radiation across the visible spectrum, resulting in a warming effect (Bond et al., 2013). The co-emission of BC and OC can lead to internally mixed particles, in which the OC coating can enhance particle absorption through lensing effects (Bond and Bergtrom, 2006; Schnaiter et al., 2005). Some organic matter containing specific functional groups (e.g. nitrated/polycyclic aromatics, phenols) can itself absorb radiation in the short wavelength visible and UV wavelengths (Hoffer et al., 2006; Jacobson, 1999) and is referred to as brown carbon (BrC). As biomass burning is a significant source of BrC, the optical properties of biomass burning particles need to be further understood. Field works have been conducted to measure the light absorption enhancement by particle coatings in different areas (Chan et al., 2011; Nakayama et al., 2014). The degree to which particles absorb light depends on their composition, shape, and mixing state. Researches on chemical composition and mixing state of biomass burning particles have been done by our group members previously (Huo et al., 2016; Zhai et al., 2015). However, it remains unclear how mixing states and chemical composition of biomass burning particles influence their morphology and optical properties.

Particles emitted from biomass burning are generally composed of a mixture of spherical and non-spherical particles and chain aggregates (Martins et al., 1998). Scanning electron microscopy (SEM) as well as transmission electron microscopy (TEM) are common techniques widely used to investigate the morphology of biomass burning particles (China et al., 2013; Giordano et al., 2015; Hopkins et al., 2007). However, these methods are unable to provide continuous "on-line" information and suffer from limitations arising from primary particle overlap, screening effects, and cluster anisotropy (Wentzel et al., 2003). Effective density is a good predictor for the complex properties of biomass burning particles (Pitz et al., 2008) and is often used to convert particle size distributions into mass loading (Schmid et al., 2007). Variations in particle effective density can be used to follow compositional transformations during chemical reactions (Katrib et al., 2005). Online measurements which provide real-time monitoring of particle effective density variation have been developed. Kelly and McMurry (1992) developed a density measurement technique based on the selection of a monodisperse aerosol with a Differential Mobility Analyzer (DMA) followed by classification according to aerodynamic diameter with an impactor. McMurry et al. (2002) reported a technique to determine size-resolved effective density based on using an Aerosol Particle Mass analyzer (APM) to measure the mass of particles that had been classified according to electrical mobility by a DMA. The DMA-APM method has been applied extensively in field studies as well as laboratory experiments (Hu et al., 2012; Barone et al., 2011). However, few measurements of the

effective density of biomass burning particles have been done due to the lack of accompanying on-line chemical information.

Mixing state of individual particle can be very different caused by the chemical composition, aging degree, etc., which greatly influence the morphology and optical property of particles. Thus, distinctions among particles might be omitted by bulk measurements. Single particle mass spectrometry techniques have been utilized to measure the chemical composition, size, density, and shape of individual particles. Spencer et al. (2007) utilized a DMA-ultrafine aerosol time-of-flight mass spectrometer (UF-ATOFMS) system to detect the effective density and chemical composition simultaneously of ambient aerosol at single-particle level. The comprehensive information about single particles could help to elucidate the morphology, mixing state, and sphericity of biomass burning particles.

The chemical composition, morphology, and optical properties of particles are usually interrelated. Biomass burning particle is a complex mixture of organic and inorganic species, including strongly light-absorbing BC and BrC. Size-resolved or even single particle level information on the morphology, chemical composition, and optical properties of biomass burning particles are necessary to have a better understanding of the correlations among these physiochemical properties. In this study, laboratory experiments were conducted on rice straw combustion, a main source of biomass burning particles in Southern China. The size-resolved effective density of biomass burning particles was measured by two different methods. One was based on a DMA-APM-Condensation Particle Counter (CPC) system. For the other method, the mobility size-selected particles by a DMA were transported into a Single Particle Aerosol Mass Spectrometer (SPAMS), where the vacuum aerodynamic diameter and chemical composition of individual particles were measured. Size-resolved optical properties of biomass burning particles were also measured by Cavity Attenuated Phase Shift spectroscopy (CAPS). A thermodenuder (TD) was used to help analyze the mixing state of particles by removing the volatile compounds and leaving behind the less volatile species based on the vaporization temperature of materials. The purpose of our study was to add physicochemical knowledge regarding biomass burning particles which is an important aerosol source globally.

2 Experiments

2.1 Laboratory-made biomass burning particles

Rice straw, a typical type of crop residue in Southern China, was taken as the representative biomass burning material in our experiment. The self-designed combustion setup was introduced in previous work (Huo et al., 2016). Briefly, the rice straws collected in rural residential area in Shanghai were dehydrated for 24 h at $100^{o}C$ in an oven prior to combustion. Five replicate tests of straw-burning were conducted for each experiment. For each test, ~ 50g of dried rice straws were burned in a combustion stove at a flaming condition. The emitted smoke was introduced into a 4.5 m^3 (in volume) chamber with a flowrate of 50 L/min. Ambient air was introduced though a high efficiency particulate air filters to maintain the ambient

pressure. The particles in chamber were then introduced into the measurement system through a silica gel type diffusion drier (shown in Figure 1).

2.2 Single particle mass spectrometry

A Single Particle Aerosol Mass Spectrometer (SPAMS) (Hexin Analytical Instrument Co., Ltd) was deployed to examine the aerosol chemical composition and aerodynamic diameter at single-particle level. Detailed information on the SPAMS has been described elsewhere (Li et al., 2011). Briefly, particles in the size range of 0.2-2.0 μm are first drawn into the vacuum through an Aerodynamic Focusing Lens. Each particle is accelerated to a size-dependent aerodynamic velocity which is calculated based on two orthogonally oriented continuous lasers (Nd: YAG, 532 nm). The two lasers are fixed at a 6 cm distance and the delay of the scatter light is collected by two photomultiplier tubes (PMT). When a particle arrives at the ion source region, a pulsed desorption/ionization laser (Qswitched Nd: YAG, 266 nm) is triggered. Ions are recorded by a bipolar time-of-flight spectrometer, which records both positive and negative mass spectra for each single particle. In this work, the power of desorption /ionization laser was set to ~0.6 mJ per pulse. The aerodynamic diameter measurement is calibrated with curves generated by monodisperse polystyrene latex spheres (Nanosphere Size Standards, Duke Scientific Corp.) with known diameters (0.2-2.0 μm).

All single particle mass spectra acquired were converted to a list of peaks at each m/z by setting a minimum signal threshold of 30 arbitrary units above the baseline with TSI MS-Analyze software. The resulting peak lists together with other SPAMS data were imported into YAADA (version 2.11, www.yaada.org), a software toolkit for single-particle data analysis written in Matlab (version R2011b). In this work, a total of 10220 biomass burning particles were chemically analyzed according to their positive and negative ion spectra, accounting for about 48 % of all sized particles. According to the similarities of the mass-to-charge ratio and peak intensity, the biomass burning particles were classified using an adaptive resonance theory-based clustering method (ART-2a) (Song et al., 1999). Base on previous work (Huang et al., 2013; Spencer et al., 2007), parameters for ART-2a used in this work such as vigilance factor, learning rate, and iterations were 0.85, 0.05, and 20, respectively. The particle clusters resulting from ART-2a were then grouped into 6 particle types based on the mass spectral patterns and chemical similarities. The name of a particle type reflects the dominant chemical species.

2.3 Effective density measurements

2.3.1 Theoretical calculation and methods

Particle density (ρ_p) is referenced to the volume equivalent diameter (d_{ve}) which is defined as the diameter of a spherical particle with the same volume as the particle under consideration. Particle density can be derived as follows, where m_p is the particle mass:

$$\rho_p = \frac{m_p}{\frac{\pi}{6}d_{ve}{}^3} \tag{1}$$

When particles are not spherical, the "effective density", not necessarily a true measurement of particle density is derived. Various definitions of effective density are provided in the literature, and a review of these definitions is given by DeCarlo et al. (2004). Different definitions may aim to present different values for a given particle. It is important to understand the derivation, calculation, and measurement for one method of particle effective density.

(1) DMA-APM-CPC system

The effective density of a particle can be calculated by combining mobility and mass measurements under the assumption that the particle is spherical, thus its physical diameter equals to the electrical mobility diameter (d_m) measured by a DMA.

The effective density (ρ_{eff}^{I}) can be calculated by the following equation:

$$\rho_{eff}^{I} = \frac{m_p}{\frac{\pi}{6}d_m^3} \tag{2}$$

where m_p stands for particle mass obtained by an APM. In our work, we selected biomass burning particles with mobility diameters of 50 nm, 100 nm, 200 nm, and 400 nm and determined their effective density using the DMA-APM-CPC system.

(2) DMA-SPAMS system

Another approach of deriving effective density is through a combination of mobility and aerodynamic measurements. Simultaneously measuring the particle electrical mobility diameter (d_m) by DMA and the vacuum aerodynamic diameter (d_{va}) by SPAMS allows for the determination of particle effective density (ρ_{eff}^{II}) by the following equation:

$$\rho_{eff}^{II} = \frac{d_{va}}{d_m}\rho_0 \tag{3}$$

where ρ_0 is the standard density (1.0 g/cm^3). In this study, since particles smaller than 200 nm may not scatter sufficient light to be detected by SPAMS and the number concentration of biomass burning particles above 400 nm was low (shown in Figure S1), we selected 200 nm and 400 nm particles by DMA and then introduced them into SPAMS.

(3) Shape factor calculation

The shape of particles can influence the optical properties and can reflect the mixing state of particles to some degree. It is possible to extract the shape information based on the measurements above.

The relationship between the volume equivalent diameter (d_{ve}) and mobility diameter (d_m) is shown in the following equation:

$$\frac{d_m}{C_c(d_m)} = \frac{d_{ve}\chi}{C_c(d_{ve})} \tag{4}$$

where χ is the shape factor, the ratio of the resistance force on the nonspherical particle to the resistance force on its volume equivalent sphere (Hinds, 1999). The χ

206 value equals 1 for spherical particles and is greater than 1 for nonspherical/irregular
207 particles.

208 *Cc* is the Cunningham Slip Correction Factor parameterized as:

209
$$Cc(d) = 1 + \frac{2\lambda}{d}[\alpha + \beta \exp(-\gamma \frac{d}{2\lambda})] \tag{5}$$

210 where d is the particle diameter (d_m or d_{ve}) and λ is the mean free path of gas
211 molecules. The empirical constants α, β, and γ are 1.142, 0.558, and 0.999
212 respectively (Allen and Raabe, 1985).

213 The vacuum aerodynamic diameter (d_{va}) is related to the volume equivalent
214 diameter (d_{ve}) by:

215
$$d_{va} = \frac{\rho_p}{\rho_0} \frac{d_{ve}}{\chi} \tag{6}$$

216 As the measurements of mobility and aerodynamic diameters are readily
217 available, we assumed the error was in the particle mass measurement if the measured
218 ρ_{eff}^{II} is used to replace ρ_{eff}^{I} in Equation (2) (Decarlo et al., 2004). With assumed
219 particle density (ρ_p) and known particle mass (m_p) measured by an APM, a calculated
220 d_{ve} could be obtained using Equation (1). Though ρ_p was unknown, it would be
221 canceled out later. Using the same d_{ve} and for any shape factor (χ), a calculated d_m and
222 d_{va} was obtained by Equation (4) and (6), respectively. Thus, ρ_{eff}^{II} could be obtained
223 by the calculated d_m and d_{va} and an estimated m_p was calculated by replacing ρ_{eff}^{I} by
224 ρ_{eff}^{II} in Equation (2). We then calculated the ratio of the estimated m_p to the exact m_p
225 as a function of d_m and χ (shown in Figure S4, discussed in Section 3.1.5).

226 **2.3.2 Instrumentation for effective density measurements**

227 The size distribution of biomass burning particles was detected by a Scanning
228 Mobility Particle Sizer (SMPS) consisting of a Differential Mobility Analyzer (DMA,
229 Model 3080, TSI Inc.) and a Condensation Particle Counter (CPC, Model 3775, TSI
230 Inc.). An Aerosol Particle Mass analyzer (APM, Model 3601, Kanomax Inc.) was
231 used to classify aerosol particles according to their mass-to-charge ratio. The detailed
232 information of the APM classification principle was previously reviewed by Tajima et
233 al. (2011). Briefly, particles were size-selected by DMA after being charged with a
234 Kr-85 neutralizer. Particles with a known size were then introduced into APM. When
235 the radial electrical and centrifugal forces were in balance, particles passed through
236 the rotating cylinders to CPC. Mass distribution was obtained by voltage scanning and
237 particle counting.

238 **2.4 Optical measurements**

239 Cavity Attenuated Phase Shift (CAPS) spectroscopy (Shoreline Science Research Inc.)
240 was used to determine the particle extinction and scattering coefficient. Detailed
241 information on the CAPS is available in Onasch et al. (2015). Briefly, a square-wave

modulated light-emitting diode (LED) is transmitted through an optical cavity cell. A sample cell incorporating two high reflectivity mirrors (R~0.9999) with a vacuum photodiode detector (Hamamatsu R645) centers at the wavelength of the LED. The particle extinction coefficient [$b_{ext}(\lambda)$] can be obtained from the changes in the phase shift of the distorted waveform of the LED. An integrating nephelometer using a 10 cm diameter integrating sphere is operated to measure the scattering coefficient [$b_{scat}(\lambda)$]. Particles are illuminated by the collimated light beam which has measured the extinction. The scattered light of particles is collected at all angels by the integrating sphere. A PMT (H7828-01, Hamamatsu) with a high voltage power supply and an amplifier records the scattered light. In this work, we used two CAPSs with the LED light sources at wavelength of 450 nm and 530 nm to detect the optical properties of biomass burning particles, respectively.

2.5 Thermodenuder

A thermodenuder (TD, Model 3065, TSI Inc.) was utilized to separate volatile and less volatile species of biomass burning particles at specific temperatures. The TD consists of a 40 cm long desorber section and a 70 cm long adsorption tube. The sample can be heated up to 400 ^{o}C in the desorber section while we selected 150 ^{o}C and 300 ^{o}C in this work. The adsorption tube is surrounded by an annular bed of activated carbon which adsorbs the evaporated gas-phase compounds, leaving behind the less volatile fractions. With a flowrate of 0.6 L/min, the residence time of particles in the TD heating section was approximately 9 s in this work.

The particle number fractions after heating do not necessarily represent the actual number fractions before heating as some of the particles can evaporate completely. Besides, particle loss could be produced both in the TD heating and adsorption section due to thermophoretic forces and diffusion, respectively (Philippin et al., 2004). On account of the quantitative measurements of optical properties, particle loss could lead to the underestimate of b_{ext} and b_{scat}.

Sodium chloride (NaCl) aerosol produced by a single-jet atomizer (Model 9302, TSI Inc.) was used to determine the transport efficiency (η) in TD. The transport efficiencies of NaCl of different electric mobility diameters selected by DMA (d_m: 50, 100, 200, and 400 nm) at a range of temperatures (T_i: 20, 150, and 300 ^{o}C) are shown in Figure S2. In TD, η decreased with increasing T_i and decreasing d_m, which is consistent with the result in Philippin et al. (2004). The measured η were used to correct the particle number concentration in the calculation of all the measurements related to the thermal-denuded process.

3 Result and discussion

3.1 Size-resolved effective density

3.1.1 Effective density from DMA-APM-CPC measurements (ρ_{eff}^{I})

The effective density of particles, measured using the DMA-APM-CPC system (ρ_{eff}^{I}),

281   provided useful information on the mixing state of particles. A Gaussian model was
282   applied to determine the effective densities of the biomass burning particles selected
283   by DMA (shown in Figure 2). The density distribution of 50 nm (d_m) particles showed
284   a single peak profile with a peak value of 1.17 g/cm^3 (Table S1). Two possible factors
285   could be inferred from this feature: a nearly-monodisperse aerosol effective density
286   distribution or a juncture of two modes with very close peak values. Biomass burning
287   particles contain highly agglomerated structures like soot (Martins et al., 1998).
288   Although the material density of black carbon (BC) is ~1.8 g/cm^3 (Bond and
289   Bergstrom, 2006), fresh BC particles with an aggregate structure can have an effective
290   density less than 1.0 g/cm^3 (Rissler et al., 2014). The density of organic matter varies
291   in the range of 1.2-2.0 g/cm^3 depending on sources (Hand et al., 2010; Turpin and Lim,
292   2001). Since particles of 50 nm have the possibility of containing organic matter
293   rather than BC alone, the apparent single-peak density distribution of these particles
294   was more likely due to the combination of two modes representing BC and organic
295   particles respectively (as the dash lines shown in Figure 2). The thermal desorption
296   method can help to explain the mixing state of 50 nm particles which will be
297   discussed in Section 3.1.3.

298   The density distribution of 100 nm particles exhibited a peak at 1.45 g/cm^3 at
299   room temperature, which suggests that these particles were dominated by organic
300   matter. However, less-massive composition with effective density of 0.9-1.1 g/cm^3
301   was also obtained for 100 nm particles. This range is identical with the density of
302   fresh BC with aggregate structure. The bi-modal distribution of the density profile of
303   100 nm particles suggests that BC was partly externally mixed with other components
304   in ultrafine particles from biomass burning emissions. Similar result has been found
305   by Lack et al. (2012) and Adachi et al. (2011). The external mixing of BC and organic
306   particulate matter was evident in the density distribution of 200 nm particles as well
307   (Figure 2). For 400 nm particles, besides a dominant density mode at 1.34 g/cm^3, a
308   relative weak mode with effective density of 1.92 g/cm^3 was observed. Previous
309   studies have shown that potassium chloride crystals, which have a material density of
310   ~ 1.99 g/cm^3 (Lide, 2008), were observed in the TEM of fresh biomass burning
311   particles (Li et al., 2015). Evidence of external mixing sodium and potassium salts in
312   ambient environment was also observed by single particle mass spectrometry in
313   previous work (Zauscher et al., 2013; Bi et al., 2011). A recent work performed by
314   Lee et al. (2016) reported that K$^+$ was not uniformly mixed in biomass burning
315   particles with less than 20% particles containing high K$^+$ content. Thus, we estimate
316   that the mode at 1.92 g/cm^3 was associated with KCl, and possibly KSO$_4$ and KNO$_3$,
317   and that these crystalline species were more likely externally mixed with organic
318   matter in biomass burning particles. The similar results of the externally mixed
319   aerosol population was observed by Moffet et al. (2008) with a wide range of
320   densities (1.1-3.4 g/ cm^3).

321   Though freshly emitted, biomass burning particles can be coated by secondary
322   species, such as ammonium nitrate and ammonium sulfate, pronouncedly in a very
323   short period (Leskinen et al., 2007). The bulk densities of ammonium nitrate and
324   ammonium sulfate are ~1.75 g/cm^3. The differences in the peak values of the

325 dominant mode observed for 50-400 nm particles are associated with the composition
326 and morphology of particles. Different proportions of the same material can lead to
327 differences in particle effective density. The dominant modes for biomass burning
328 particles in the size range of 50-400 nm (Figure 2) could be a mixture of similar
329 composition (BC, OC, potassium salts and secondary inorganic species) but different
330 proportions. Detailed information and discussion about the particle composition can
331 be found in Section 3.2.

332 **3.1.2 Effective density from DMA-SPAMS measurements (ρ_{eff}^{II})**

333 The vacuum aerodynamic size distributions of 200 nm and 400 nm electrical mobility
334 selected biomass burning particles are shown in Figure 3. The dominant mode for the
335 200 nm mobility selected particles was 280 nm in vacuum aerodynamic diameter with

336 an effective density (ρ_{eff}^{II}) of 1.40 g/cm^3 and a second mode at 360 nm (d_{va}) with an

337 effective density of 1.80 g/cm^3. This is quite consistent with the result from the
338 DMA-APM-CPC method. The less intense mode at 520 nm (d_{va}) should be due to
339 doubly charged particles (Spencer et al., 2007). For 400 nm mobility selected particles,
340 the dominant mode in aerodynamic diameter was 540 nm with an effective density of
341 1.35 g/cm^3. Since the less massive modes at 660 nm and 840 nm were not in the range
342 of doubly charged particles, these two modes were singly charged particles with
343 effective density of 1.65 and 2.10 g/cm^3, respectively. The single-particle level
344 chemical composition of biomass burning particles will be discussed below.

345 Figure S3 summarizes that the average effective densities (ρ_{eff}^{I} & ρ_{eff}^{II}) of

346 biomass burning particles that were size-selected at 6 different mobility diameters.
347 Note that the density distributions of the 300 nm and 350 nm (d_m) particles are not
348 contained in Figure 2 since they were similar to those of the 200 nm and 400 nm (d_m)
349 particles. The 50 nm biomass burning particles had the lowest effective density of
350 1.15$\pm$0.23 g/cm^3 which could be due to the aggregate structure of black carbon.
351 Compared with 50 nm (d_m) particles, the effective density of 100 nm particles was
352 higher (1.45$\pm$0.15 g/cm^3). Since the sampling limitation of SPAMS was 200 nm,

353 ρ_{eff}^{II} was derived only for particles in the size range of 200-400 nm (d_m). Overall, these

354 two methods had consistent results. The differences between the average values from the two

355 methods were less than 8% for all particle sizes. We noticed that ρ_{eff}^{II} were generally smaller

356 than ρ_{eff}^{I}, which could be due to the systematic error from different measurements.

357 **3.1.3 Thermal-denuded particle effective density**

358 The average density distributions of 50-400 nm (d_m) biomass burning particles after
359 heating at 150°C and 300°C, respectively, are shown in Figure 2. It is worth noting
360 that the thermal-denuded particle density distribution here was not from the particles

with the same original dried-particle diameter. However, our observations are still meaningful since the evolution trends of density distribution after heating were similar despite of the particle size.

After heating by TD, the bi-modal density distributions of biomass burning particles became more pronounced. At 150 ^{o}C, the effective density mode with peak at ~1.0 g/cm^3 protruded for the whole size range of 50-400 nm particles. The separation of the peaks after heating suggested that the some less volatile BC or soot with effective density of ~1.0 g/cm^3 was possibly externally mixed with other compositions. The dominant density peak values for 50, 100, 200, and 400 nm particles at 150 ^{o}C were 1.64-1.80 g/cm^3. Li et al. (2016) reported that the density of organic matter vaporized at 150 ^{o}C was 0.61-0.90 g/cm^3. The increase of the dominant density peak value (1.34-1.45 g/cm^3 for unheated vs. 1.64-1.80 g/cm^3 for 150 ^{o}C heated) could be due to the volatilization of organics with low effective density. The dominant density peak values of 50-400 nm particles at 300 ^{o}C were 1.75-2.04 g/cm^3. The volatilization temperatures of ammonium nitrate and ammonium sulfate are reported to be ~48-89 ^{o}C and ~178-205 ^{o}C, respectively (Johnson et al., 2004a; Johnson et al., 2004b). Thus, the fractions of ammonium nitrate and ammonium sulfate should be small at 300 ^{o}C. The increase of dominant density peak value for 50-400 nm biomass burning particles upon heating could be due to the vaporization of volatile organics with low effective density and secondary inorganic species such as NH_4NO_3 and $(NH_4)_2SO_4$ with density of ~1.75 g/cm^3. Besides, Bond and Bergstrom (2006) reported that the density of light-absorbing carbon should be 1.7-2.1 g/cm^3 which is quite high compared with the density of the volatile organics (0.61-0.90 g/cm^3). Saleh et al. (2014) had shown that the light-absorbing organics in biomass burning particles were extremely low volatility organic compounds. Thus, we assume these extremely low volatility organics should play an important role in the dominant effective density mode at 300°C.

Upon heating, the density mode of KCl and partly K_2SO_4 at ~2.0 g/cm^3 was ambiguous as the dominant mode shifted right and overlapped with the KCl mode (dash lines shown in Figure 2). However, at 300 ^{o}C, the dominant mode of 400 nm particles was at 2.05 g/cm^3 which fitted the density of potassium salts, indicating the main material of 400 nm heated (~800 nm unheated, detected by a tandem DMAs) biomass burning particles should be potassium salts with vaporization temperatures above 700°C (Knudsen et al., 2004).

With heating by TD, the aerodynamic size distributions of 200 nm and 400 nm electrical mobility size-selected biomass burning particles at 300 ^{o}C are shown in Figure 3. The increase of ρ_{eff}^{II} upon heating was consistent with that of ρ_{eff}^{I}.

3.1.4 Shape factor

The shape of particles has been suggested to play an important role in their optical properties (Zhang et al., 2008) and mixing state (China et al., 2013). Shape factor was introduced to account for the ratio of the drag forces on a particle due to nonspherical/irregular shape. Shape factor, which can be extracted based on the

403 measurement of particle density and mass has been introduced in Section 2.3.1.

404   We calculated the ratio of the estimated m_p to the exact m_p as a function of d_m

405 and χ (shown in Figure S4). For nonspheical particles ($\chi > 1$), the estimated mass was

406 larger than the actual mass. We calculated the estimated mass using the exact ρ_{eff}^{II}

407 measured by the DMA-SPAMS to replace the ρ_{eff}^{I} in Equation (2) as well. The ratios

408 of the estimated mass by this mean to the exact mass for 200, 300, 350, and 400 nm

409 mobility selected particles were 1.4, 1.3, 1.3, and 1.2 respectively (red dots in Figure

410 S4). Thus, we could estimate the χ of the particle measured using the DMA-SPAMS

411 in the size range of 200-400 nm. Totally, the χ of 200-400 nm biomass burning

412 particle in this work exceeded 1.2 (~1.2-2.2). The χ decreased with the increase of d_m

413 while the effective density showed the same trend. The more regular shape and lower

414 effective density of 400 nm particles compared with that of 200 nm particles could be

415 due to the particle chemical composition and particle voids (discussed in Section 3.2).

416 **3.2 Size-resolved chemical composition**

417 The mass spectra of individual biomass burning particles have been studied in

418 previous work (Silva et al., 1999; Zauscher et al., 2013). Based on the mass spectra of

419 single particles, the biomass burning particles were classified into 6 particle types: 1)

420 BB-CN: biomass burning (BB) particles with a strong CN^- (m/z -26 [CN^-]) peak; 2)

421 BB-EC: BB particles with strong elemental carbon clusters ($C_n^{+/-}$); 3) BB-Nitrate: BB

422 particles with strong nitrate (m/z -46[NO_2^-], -62[NO_3^-]) signals; 4) BB-Sulfate: BB

423 particles with strong sulfate (m/z -97[HSO_4^-]) signals; 5) BB-KCl: BB particles with

424 strong potassium chlorine (m/z 113[K_2Cl^+]) signals; and 6) BB-OC: BB particles with

425 strong organic carbon peaks (e.g., m/z 27[$C_2H_3^+$], 37[C_3H^+], 43[$C_3H_7^+$], 51[$C_4H_3^+$], et

426 al.). The naming of the chemical classes is based on some of the dominant chemical

427 species in an attempt to keep the names short. The mass spectra for each particle type

428 are presented in Figure S5. The percentages of 6 particle types in different modes of

429 aerodynamic size distribution for 200 nm and 400 nm mobility selected particles are

430 shown in Figure 3. For 200 nm mobility selected particles, the dominant particle types

431 were BB-EC and BB-CN. The percentages of particle types within the two

432 aerodynamic modes differ slightly. Compared with the first mode, the second mode

433 contains more BB-CN (24.4% vs. 29.6%), more BB-KCl (1.0% vs. 4.3%) and less

434 BB-EC (32.2% vs. 22.9%). We supposed that the density of each particle type largely

435 depended on the dominant species. The exact effective density of each particle type

436 could not be obtained directly while the relative value compared with other particle

437 types could be inferred from the material density of dominant species. For example,

438 the BB-KCl type might have higher effective density compared with others since the

439 dominant composition KCl has a material density of ~1.99 g/cm^3 (Lide, 2008). The

440 increased BB-KCl type and the decrease of BB-EC (~1.0 g/cm^3) resulted in a higher

441 effective density in the second mode than the first mode.

442   The fractional distributions of the 6 particle types for 200 nm and 400 nm

443 mobility selected particles were apparently different (Figure 3). For 400 nm mobility

selected particles, the proportions of BB-Nitrate, BB-Sulfate and BB-KCl types were larger than those of 200 nm mobility selected particles. The dominant chemical species for BB-Nitrate and BB-Sulfate particle types could be NH_4NO_3 and $(NH_4)_2SO_4$ with material density of ~1.75 g/cm^3 (Lide, 2008). Compared with other types, BB-Nitrate, BB-Sulfate and BB-KCl were particle types with higher density. However, the effective density for 400 nm mobility selected particles was lower than that of 200 nm. In addition to the compositional differences, particle morphology could be another reason responsible for the observed differences in the effective densities between these two sizes. Indeed, it has been found that the morphology like void ratio, particle shape factor, and fractal dimension of particles all greatly affect particle effective density (DeCarlo et al., 2004). Though the shape factor discussed in Section 3.1 had shown that the 400 nm (d_m) particles had a more spherical morphology, their lower average effective density compared to smaller particles could be due to the voids in particles. Amorphous species such as NH_4NO_3 (Audebrand et al., 1997) could lead to the low effective density of particles. Thus, we supposed the lower effective density of 400 nm particles compared with 200 nm particles was caused by the large proportion of NH_4NO_3 and $(NH_4)_2SO_4$ with fluffy material properties.

For 400 nm mobility selected particles, the pie charts of particle type were almost identical for the first and second modes (as shown in Fig. 3b, 20 ^{o}C). Thus, we assume these two modes were derived from one effective density mode. The proportion of BB-KCl in the third mode at 840 nm with effective density of 2.10 g/cm^3 greatly increased compared with the first two modes (8.8%, 9.2% vs. 32.7%). The increased BB-KCl indicated that the KCl crystals were external mixed and tended to be mixed with larger size particles which were consistent with the DMA-APM-CPC result.

Upon heating by TD, the proportions of BB-CN and BB-KCl increased, indicating that these types of particles were composed of less volatile species (shown in Figure 3) (Zhai et al., 2015). At 300°C, the fractions of BB-Nitrate and BB-Sulfate decreased, consistent with the volatilization temperature ranges of ammonium nitrate (~48-89 ^{o}C) and ammonium sulfate (~178-205 ^{o}C) (Johnson et al., 2004a; Johnson et al., 2004b). The high effective density (>2.0) of biomass burning particles at 300°C could be due to the vaporization of volatile organics with low density since the BB-OC type decreased drastically after thermal treatment. Besides, the increasing proportion of BB-KCl upon heating could be another important reason for the higher effective density at 300 ^{o}C.

3.3 Size-resolved optical properties

3.3.1 Single scattering albedo (SSA)

The single scattering albedo (SSA), was calculated using the following equation:

$$SSA(\lambda) = b_{scat}(\lambda) / [b_{abs}(\lambda) + b_{sca}(\lambda)]$$

where b_{scat} is the particle light scattering coefficient, b_{abs} is the light absorption coefficient, and λ is wavelength. The light scattering and extinction coefficients (b_{ext}, $= b_{abs} + b_{sca}$) for biomass burning particles in this work were measured at 530 nm and

450 nm wavelengths using CAPSs.

The size-resolved SSAs for biomass burning particles are shown in Figure 4. Totally, the SSAs for biomass burning particles in the mobility size range of 50-400 nm varied narrowly. It's worth noting that the optical measurement was based on bulk measurement by CAPSs, which is not sensitive to the diversity of particle mixing state.

The SSA (530 nm) for 50 nm particles was the lowest (0.889 ± 0.006) as the percentage of strong light-absorbing black carbon for particles in this size range was larger (shown in Figure 3, discussed in Section 3.2). For 100-400 nm biomass burning particles, the SSAs were relatively steady ($0.897 \pm 0.006 - 0.900 \pm 0.006$).

The size-resolved SSAs at 450 nm (λ) for biomass burning particles were generally lower than those at 530 nm (λ). Previous studies have shown that biomass burning was an important source of brown carbon (BrC) which is light-absorbing in the UV-vis range (Lack and Cappa, 2010). For 50 nm (d_m) particles, the SSA ($\lambda=450$ nm) was also the lowest, due to the dominance of the strong light-absorbing BC in these particles. However, unlike the trend of size-resolved SSAs ($\lambda=530$ nm), the SSA ($\lambda=450$ nm) of 100-400 nm particles increased as the size increased. It has been shown that brown carbon arising from biomass burning is primarily composed of extremely low volatility organic compounds (Saleh et al., 2014). The CN^- in biomass burning particles is representative for some extremely low volatility nitrogen-containing organics (Zhai et al., 2015). As shown in Figure 3, compared with 400 nm particles, the proportion of organic matter (BB-CN, BB-OC) was larger for 200 nm particles. The nitrogen-containing species might indicate the existence of light-absorbing organics. The lower SSA ($\lambda=450$ nm) for 200 nm particles might indicate a larger proportion of BrC. We assumed the lower SSA ($\lambda=450$ nm) for 100 nm performed in a similar way with a larger proportion of BrC.

3.3.2 Ångström absorption exponent (AAE)

To investigate the wavelength dependence of the absorption coefficients, we determined the Ångström absorption exponent (AAE) based on absorption measurements at two different wavelengths (λ_1 & λ_2) using the following equation:

$$\text{AAE} (\lambda_1 / \lambda_2) = - \ln[\ b_{abs} (\lambda_1) /\ b_{abs} (\lambda_2)] / \ln(\lambda_1 / \lambda_2)$$

The AAE in this work was calculated from the light absorption coefficients at wavelengths of 450 nm and 530 nm measured by the CAPSs. The uncertainties in the calculated AAE values can be caused by the uncertainties in the calibration factors of CAPSs. The size-resolved AAEs for biomass burning particles are shown in Figure 4. Black carbon is highly absorbing in the visible spectrum with little variation with wavelength and shows an AAE of ~1.0 (Bergstrom et al., 2002). As brown carbon species absorb light in the UV-vis range, BrC-containing particles usually exhibit an AAE above 1 (Martinsson et al., 2015). Lack and Cappa (2010) used modeling to calculate AAE values and suggested that particles with AAE exceeding 1.6 should be classified as BrC. In our study, the AAE values of particles in the size range of 50-400 nm were higher than 1.6, indicating that they were BrC-containing particles from biomass burning. Among all sizes, the AAE of 50 nm biomass burning particles was

the lowest (~5.8) while that of 100 nm particles was the highest (~6.3). The main light-absorbing functional groups in the UV-vis range is conjugated double bond (Laskin et al., 2015). BB-CN and BB-OC particle types identified by mass spectra in our work tended to contain more large molecules of BrC with light-absorbing functional groups. We noticed that the proportion of BB-OC type species was larger in 200 nm particles (Figure 3) and with higher AAE value, compared with 400 nm particles. Thus, we suppose the highest AAE value observed for 100 nm particles might be the result of the largest BrC proportion.

The SSA and AAE values of total biomass burning particles are shown in Table S2. The decrease of SSA values upon heating was due to the vaporization of secondary inorganic species like NH_4NO_3 and less absorbing organics. The AAE values for all particles at 150 ^{o}C and 300 ^{o}C were ~19% and ~64%, lower than those at room temperature (20 ^{o}C). The significant decrease of AAE at 300 ^{o}C could be due to the vaporization of light-absorbing organics in the temperature range of 150-300 ^{o}C. However, the AAE value at 300 ^{o}C was still above 1.6, indicating the presence of extremely low volatility light-absorbing organics in biomass burning particles. McMeeking et al. (2014) found that the strongly light-absorbing biomass burning particles tended to have a weak wavelength dependent absorption while the weakly light-absorbing particles tended to have a strong wavelength dependent absorption, which is consistent with our results. In this work, the high values of AAE (~ 6.23) and SSA (~0.89, at 530 nm) suggested the light absorbing of rice straw burning particles were relatively weak compared to the particles emitted from other types of biofuels.

4 Conclusions

As a major primary source of aerosols, biomass burning emissions significantly impact the global radiative budget. It is important to understand the physical and chemical properties of biomass burning particles, as well as their links to optical properties. In this work, rice straw was combusted as a representative material of biomass burning in Southern China. A series of comprehensive methods was used to detect the size-resolved chemical composition, effective density, and optical properties of the particles emitted from the burns.

Two methods were utilized to measure the effective density of the biomass burning particles. The DMA-APM-CPC system, which has been widely used in chamber and field work, offered size-resolved information on the particle effective density. The DMA-SPAMS system provided physical property and chemical composition at single-particle level. The 50 nm (d_m) biomass burning particles had the lowest effective density of 1.15 ± 0.23 g/cm^3, which was due to the large proportion of fractal black carbon. The apparent single-peak density distribution of 50 nm particles was due to the combination of two modes (BC and organic matter, respectively). The independent modes at 0.9-1.1 g/cm^3 shown in the density distribution of 100 nm and 200 nm particles and ~1.92 g/cm^3 mode shown in that of 400 nm particles indicated that BC and crystalline species such as KCl in fresh biomass burning particles tended to be externally mixed with organic carbon. With heating by TD, the separation of the effective density distribution modes testified the

573 presence of BC, potassium salts and less volatile OC in the biomass burning particles.

574   The effective density measured by DMA-SPAMS system was consistent with the
575 result by DMA-APM-CPC method. The dominant modes in the effective density
576 distributions of 200 nm and 400 nm mobility selected particles were 1.40 g/cm^3 and
577 1.35 g/cm^3, respectively. The crystalline KCl with an effective density of 2.10 g/cm^3
578 (with BB-KCl type accounting for 32.7%) was observed in the density distribution for
579 400 nm particles measured by DMA-SPAMS. The proportions of BB-Nitrate,
580 BB-Sulfate, and BB-KCl types in 400 nm mobility selected particles were larger than
581 those in 200 nm mobility selected particles. Compared with 200 nm particles, 400 nm
582 particles showed more spherical morphology but lower effective density, which could
583 be due to the larger proportion of low density organics and amorphous NH_4NO_3.

584   The size-resolved extinction and scattering coefficients were measured by
585 CAPSs at wavelengths of 450 nm and 530 nm. The SSA (λ=530 nm) for 50 nm
586 particles was the lowest (0.889±0.006) because of the presence of a larger percentage
587 of the strongly light-absorbing black carbon particles in this size mode. The
588 size-resolved SSAs (λ=450 nm) for biomass burning particles were generally lower
589 than the SSAs (λ=530 nm). The AAE values in the size range of 50-400 nm particles
590 were all above 1.6, indicating the significant presence of brown carbon in all sizes.
591 The AAE value was the lowest for 50 nm particles (~5.8) while was the highest for
592 100 nm particles (~6.3). Compared with 400 nm particles, the proportions of BB-OC
593 and BB-CN, the extremely low volatility organic compounds, were larger for 200 nm
594 particles which might indicate a higher possibility for the existence of light-absorbing
595 organics. Our work emphasizes on the complex mixing states of aerosols from
596 primary source. Further research on how particle morphology affects the optical
597 properties of biomass burning particles is needed.

Acknowledgements

599   This work was supported by the National Natural Science Foundation of China
600 (91544224, 21507010), the Ministry of Science & Technology of China
601 (2012YQ220113-4), the Science & Technology Commission of Shanghai
602 Municipality (14DZ1202900), and the Changjiang Scholars program of the Chinese
603 Ministry of Education.

References

605 Adachi, K., and Buseck, P. R.: Atmospheric tar balls from biomass burning in Mexico,
606   J. Geophys. Res.-Atmos., 116, doi:10.1029/2010jd015102, 2011.
607 Allen, M. D., and Raabe, O. G.: Slip correction measurements of spheical solid
608   aerosol-particles in an improved millikan apparatus, Aerosol Sci. Technol., 4,
609   269-286, doi:10.1080/02786828508959055, 1985.
610 Andreae, M. O., and Merlet, P.: Emission of trace gases and aerosols from biomass
611   burning, Global Biogeochem. Cy., 15, 955-966, doi:10.1029/2000gb001382, 2001.
612 Audebrand, N., Auffredic, J. P., and Louer, D.: Thermal decomposition of cerous
613   ammonium nitrate tetrahydrate studied with temperature-dependent X-ray powder
614   diffraction and thermal analysis, Thermochim. Acta, 293, 65-76, doi:

615   10.1016/s0040-6031(97)00064-6, 1997.

616 Barone, T. L., Lall, A. A., Storey, J. M. E., Mulholland, G. W., Prikhodko, V. Y.,
617   Frankland, J. H., Parks, J. E., and Zachariah, M. R.: Size-resolved density
618   measurements of particle emissions from an advanced combustion diesel engine:
619   effect of aggregate morphology, Energ. Fuel., 25, 1978-1988,
620   doi:10.1021/ef200084k, 2011.

621 Bergstrom, R. W., Russell, P. B., and Hignett, P.: Wavelength dependence of the
622   absorption of black carbon particles: Predictions and results from the TARFOX
623   experiment and implications for the aerosol single scattering albedo, J. Atmos. Sci.,
624   59, 567-577, doi: 10.1175/1520-0469(2002)059<0567:wdotao>2.0.co;2, 2002.

625 Bi, X. H., Zhang, G. H., Li, L., Wang, X. M., Li, M., Sheng, G. Y., Fu, J. M., and
626   Zhou, Z.: Mixing state of biomass burning particles by single particle aerosol mass
627   spectrometer in the urban area of PRD, China, Atmos. Environ., 45, 3447-3453, doi:
628   10.1016/j.atmosenv.2011.03.034, 2011.

629 Bond, T. C., Streets, D. G., Yarber, K. F., Nelson, S. M., Woo, J.-H., and Klimont, Z.:
630   A technology-based global inventory of black and organic carbon emissions from
631   combustion, J. Geophys. Res- Atmos., 109, doi: 10.1029/2003jd003697, 2004.

632 Bond, T. C., and Bergstrom, R. W.: Light absorption by carbonaceous particles: An
633   investigative review, Aerosol Sci. Technol., 40, 27-67, doi:
634   10.1080/02786820500421521, 2006.

635 Bond, T. C., Doherty, S. J., Fahey, D. W., Forster, P. M., Berntsen, T., DeAngelo, B. J.,
636   Flanner, M. G., Ghan, S., Karcher, B., Koch, D., Kinne, S., Kondo, Y., Quinn, P. K.,
637   Sarofim, M. C., Schultz, M. G., Schulz, M., Venkataraman, C., Zhang, H., Zhang,
638   S., Bellouin, N., Guttikunda, S. K., Hopke, P. K., Jacobson, M. Z., Kaiser, J. W.,
639   Klimont, Z., Lohmann, U., Schwarz, J. P., Shindell, D., Storelvmo, T., Warren, S.
640   G., and Zender, C. S.: Bounding the role of black carbon in the climate system: A
641   scientific assessment, J. Geophys. Res- Atmos., 118, 5380-5552, doi:
642   10.1002/jgrd.50171, 2013.

643 Cao, G., Zhang, X., Wang, Y., and Zheng, F.: Estimation of emissions from field
644   burning of crop straw in China, Chinese Sci. Bull., 53, 784-790, doi:
645   10.1007/s11434-008-0145-4, 2008.

646 Chan, T. W., Brook, J. R., Smallwood, G. J., and Lu, G.: Time-resolved measurements
647   of black carbon light absorption enhancement in urban and near-urban locations of
648   southern Ontario, Canada, Atmos. Chem. Phys., 11, 10407-10432, doi:
649   10.5194/acp-11-10407-2011, 2011.

650 Chand, D., Wood, R., Anderson, T. L., Satheesh, S. K., and Charlson, R. J.:
651   Satellite-derived direct radiative effect of aerosols dependent on cloud cover, Nat.
652   Geosci., 2, 181-184, doi: 10.1038/ngeo437, 2009.

653 China, S., Mazzoleni, C., Gorkowski, K., Aiken, A. C., and Dubey, M. K.:
654   Morphology and mixing state of individual freshly emitted wildfire carbonaceous
655   particles, Nat. Commun., 4, 2122, doi: 10.1038/ncomms3122, 2013.

656 DeCarlo, P. F., Slowik, J. G., Worsnop, D. R., Davidovits, P., and Jimenez, J. L.:
657   Particle morphology and density characterization by combined mobility and
658   aerodynamic diameter measurements. Part 1: theory, Aerosol Sci. Technol., 38,

659   1185-1205, doi: 10.1080/027868290903907, 2004.

660 Giordano, M., Espinoza, C., and Asa-Awuku, A.: Experimentally measured
661   morphology of biomass burning aerosol and its impacts on CCN ability, Atmos.
662   Chem. Phys., 15, 1807-1821, doi: 10.5194/acp-15-1807-2015, 2015.

663 Hand, J. L., Day, D. E., McMeeking, G. M., Levin, E. J. T., Carrico, C. M.,
664   Kreidenweis, S. M., Malm, W. C., Laskin, A., and Desyaterik, Y.: Measured and
665   modeled humidification factors of fresh smoke particles from biomass burning: role
666   of inorganic constituents, Atmos. Chem. Phys., 10, 6179-6194, doi:
667   10.5194/acp-10-6179-2010, 2010.

668 Hinds, W. C.: Aerosol Technology: Properties, behavior, and measurement of airborne
669   particles, Wiley, 1999.

670 Hoffer, A., Gelencsér, A., Guyon, P., Kiss, G., Schmid, O., Frank, G. P., Artaxo, P.,
671   and Andreae, M. O.: Optical properties of humic-like substances (HULIS) in
672   biomass-burning aerosols, Atmos. Chem. Phys., 6, 3563-3570, doi:
673   10.5194/acp-6-3563-2006, 2006.

674 Hopkins, R. J., Lewis, K., Desyaterik, Y., Wang, Z., Tivanski, A. V., Arnott, W. P.,
675   Laskin, A., and Gilles, M. K.: Correlations between optical, chemical and physical
676   properties of biomass burn aerosols, Geophys. Res. Lett., 34, doi:
677   10.1029/2007gl030502, 2007.

678 Hu, M., Peng, J., Sun, K., Yue, D., Guo, S., Wiedensohler, A., and Wu, Z.: Estimation
679   of size-resolved ambient particle density based on the measurement of aerosol
680   number, mass, and chemical size distributions in the winter in Beijing, Environ. Sci.
681   Technol., 46, 9941-9947, doi: 10.1021/es204073t, 2012.

682 Huang, Y., Li, L., Li, J., Wang, X., Chen, H., Chen, J., Yang, X., Gross, D., Wang, H.,
683   and Qiao, L.: A case study of the highly time-resolved evolution of aerosol
684   chemical and optical properties in urban Shanghai, China, Atmos. Chem. Phys., 13,
685   3931-3944, doi: 10.5194/acp-13-3931-2013, 2013.

686 Huo, J., Lu, X., Wang, X., Chen, H., Ye, X., Gao, S., Gross, D. S., Chen, J., and Yang,
687   X.: Online single particle analysis of chemical composition and mixing state of
688   crop straw burning particles: from laboratory study to field measurement, Front.
689   Env. Sci. Eng., 10, 244-252, doi: 10.1007/s11783-015-0768-z, 2016.

690 Jacobson, M. Z.: Isolating nitrated and aromatic aerosols and nitrated aromatic gases
691   as sources of ultraviolet light absorption, J. Geophys. Res.-Atmos., 104, 3527-3542,
692   doi: 10.1029/1998jd100054, 1999.

693 Johnson, G., Ristovski, Z., and Morawska, L.: Application of the VH-TDMA
694   technique to coastal ambient aerosols, Geophys. Res. Lett., 31,
695   doi:10.1029/2004gl020126, 2004a.

696 Johnson, G. R., Ristovski, Z., and Morawska, L.: Method for measuring the
697   hygroscopic behaviour of lower volatility fractions in an internally mixed aerosol, J.
698   Aerosol Sci., 35, 443-455, doi:10.1016/j.jaerosci.2003.10.008, 2004b.

699 Katrib, Y., Martin, S. T., Rudich, Y., Davidovits, P., Jayne, J. T., and Worsnop, D. R.:
700   Density changes of aerosol particles as a result of chemical reaction, Atmos. Chem.
701   Phys., 5, 275-291, doi: 10.5194/acp-5-275-2005, 2005.

702 Kelly, W. P., and McMurry, P. H.: Measurement of particle density by inertial

classification of differential mobility analyzer–generated monodisperse aerosols, Aerosol Sci. Technol., 17, 199-212, doi: 10.1080/02786829208959571, 1992.

Knudsen, J. N., Jensen, P. A., and Dam-Johansen, K.: Transformation and release to the gas phase of Cl, K, and S during combustion of annual biomass, Energ. Fuel., 18, 1385-1399, doi: 10.1021/ef049944q, 2004.

Lack, D. A., and Cappa, C. D.: Impact of brown and clear carbon on light absorption enhancement, single scatter albedo and absorption wavelength dependence of black carbon, Atmos. Chem. Phys., 10, 4207-4220, doi: 10.5194/acp-10-4207-2010, 2010.

Lack, D. A., Langridge, J. M., Bahreini, R., Cappa, C. D., Middlebrook, A. M., and Schwarz, J. P.: Brown carbon and internal mixing in biomass burning particles, P. Natl. Acad. Sci. USA, 109, 14802-14807, doi: 10.1073/pnas.1206575109, 2012.

Laskin, A., Laskin, J., and Nizkorodov, S. A.: Chemistry of atmospheric brown carbon, Chem. Rev., 115, 4335-4382, doi: 10.1021/cr5006167, 2015.

Lee, A. K. Y., Willis, M. D., Healy, R. M., Wang, J. M., Jeong, C.-H., Wenger, J. C., Evans, G. J., and Abbatt, J. P. D.: Single-particle characterization of biomass burning organic aerosol (BBOA): evidence for non-uniform mixing of high molecular weight organics and potassium, Atmos. Chem. Phys., 16, 5561-5572, doi: 10.5194/acp-16-5561-2016, 2016.

Leskinen, A. P., Jokiniemi, J. K., and Lehtinen, K. E. J.: Characterization of aging wood chip combustion aerosol in an environmental chamber, Atmos. Environ., 41, 3713-3721, doi: 10.1016/j.atmosenv.2006.12.016, 2007.

Li, C., Ma, Z., Chen, J., Wang, X., Ye, X., Wang, L., Yang, X., Kan, H., Donaldson, D. J., and Mellouki, A.: Evolution of biomass burning smoke particles in the dark, Atmos. Environ., 120, 244-252, doi: 10.1016/j.atmosenv.2015.09.003, 2015.

Li, C., Hu, Y., Chen, J., Ma, Z., Ye, X., Yang, X., Wang, L., Wang, X., and Mellouki, A.: Physiochemical properties of carbonaceous aerosol from agricultural residue burning: Density, volatility, and hygroscopicity, Atmos. Environ., 140, 94-105, doi:10.1016/j.atmosenv.2016.05.052, 2016.

Li, L., Huang, Z., Dong, J., Li, M., Gao, W., Nian, H., Fu, Z., Zhang, G., Bi, X., Cheng, P., and Zhou, Z.: Real time bipolar time-of-flight mass spectrometer for analyzing single aerosol particles, Int. J. Mass Spectrom., 303, 118-124, doi: 10.1016/j.ijms.2011.01.017, 2011.

Lide, D. R.: CRC handbook of chemistry and physics, CRC, Taylor and Francis, 2008.

Martins, J. V., Hobbs, P. V., Weiss, R. E., and Artaxo, P.: Sphericity and morphology of smoke particles from biomass burning in Brazil, J. Geophys. Res.-Atmos., 103, 32051-32057, doi: 10.1029/98jd01153, 1998.

Martinsson, J., Eriksson, A. C., Nielsen, I. E., Malmborg, V. B., Ahlberg, E., Andersen, C., Lindgren, R., Nystrom, R., Nordin, E. Z., Brune, W. H., Svenningsson, B., Swietlicki, E., Boman, C., and Pagels, J. H.: Impacts of combustion conditions and photochemical processing on the light absorption of biomass combustion aerosol, Environ. Sci. Technol., 49, 14663-14671, doi: 10.1021/acs.est.5b03205, 2015.

McMeeking, G. R., Fortner, E., Onasch, T. B., Taylor, J. W., Flynn, M., Coe, H., and

Kreidenweis, S. M.: Impacts of nonrefractory material on light absorption by aerosols emitted from biomass burning, J. Geophys. Res.-Atmos., 119, 2014JD021750, doi: 10.1002/2014JD021750, 2014.

McMurry, P. H., Wang, X., Park, K., and Ehara, K.: The relationship between mass and mobility for atmospheric particles: a new technique for measuring particle density, Aerosol Sci. Technol., 36, 227-238, doi: 10.1080/027868202753504083, 2002.

Moffet, R. C., Qin, X. Y., Rebotier, T., Furutani, H., and Prather, K. A.: Chemically segregated optical and microphysical properties of ambient aerosols measured in a single-particle mass spectrometer, J. Geophys. Res.-Atmos., 113, doi: 10.1029/2007jd009393, 2008.

Naeher, L. P., Brauer, M., Lipsett, M., Zelikoff, J. T., Simpson, C. D., Koenig, J. Q., and Smith, K. R.: Woodsmoke health effects: a review, Inhal. toxicol., 19, 67-106, doi: 10.1080/08958370600985875, 2007.

Nakayama, T., Ikeda, Y., Sawada, Y., Setoguchi, Y., Ogawa, S., Kawana, K., Mochida, M., Ikemori, F., Matsumoto, K., and Matsumi, Y.: Properties of light-absorbing aerosols in the Nagoya urban area, Japan, in August 2011 and January 2012: Contributions of brown carbon and lensing effect, J. Geophys. Res.-Atmos., 119, 12721-12739, doi: 10.1002/2014jd021744, 2014.

Onasch, T. B., Massoli, P., Kebabian, P. L., Hills, F. B., Bacon, F. W., and Freedman, A.: Single scattering albedo monitor for airborne particulates, Aerosol Sci. Technol., 49, 267-279, doi: 10.1080/02786826.2015.1022248, 2015.

Park, R., Jacob, D., Kumar, N., and Yantosca, R.: Regional visibility statistics in the United States: Natural and transboundary pollution influences, and implications for the Regional Haze Rule, Atmos. Environ., 40, 5405-5423, doi: 10.1016/j.atmosenv.2006.04.059, 2006.

Petters, M. D., Carrico, C. M., Kreidenweis, S. M., Prenni, A. J., DeMott, P. J., Collett, J. L., and Moosmuller, H.: Cloud condensation nucleation activity of biomass burning aerosol, J. Geophys. Res.-Atmos., 114, 16, doi: 10.1029/2009jd012353, 2009.

Philippin, S., Wiedensohler, A., and Stratmann, F.: Measurements of non-volatile fractions of pollution aerosols with an eight-tube volatility tandem differential mobility analyzer (VTDMA-8), J. Aerosol Sci., 35, 185-203, doi: 10.1016/j.jaerosci.2003.07.004, 2004.

Pitz, M., Schmid, O., Heinrich, J., Birmili, W., Maguhn, J., Zimmermann, R., Wichmann, H. E., Peters, A., and Cyrys, J.: Seasonal and diurnal variation of PM2.5 apparent particle density in urban air in Augsburg, Germany, Environ. Sci. Technol., 42, 5087-5093, doi: 10.1021/es7028735, 2008.

Rissler, J., Nordin, E. Z., Eriksson, A. C., Nilsson, P. T., Frosch, M., Sporre, M. K., Wierzbicka, A., Svenningsson, B., Londahl, J., Messing, M. E., Sjogren, S., Hemmingsen, J. G., Loft, S., Pagels, J. H., and Swietlicki, E.: Effective density and mixing state of aerosol particles in a near-traffic urban environment, Environ. Sci. Technol., 48, 6300-6308, doi: 10.1021/es5000353, 2014.

Saleh, R., Robinson, E. S., Tkacik, D. S., Ahern, A. T., Liu, S., Aiken, A. C., Sullivan,

R. C., Presto, A. A., Dubey, M. K., Yokelson, R. J., Donahue, N. M., and Robinson, A. L.: Brownness of organics in aerosols from biomass burning linked to their black carbon content, Nat. Geosci., 7, 647-650, doi: 10.1038/ngeo2220, 2014.

Schmid, O., Karg, E., Hagen, D. E., Whitefield, P. D., and Ferron, G. A.: On the effective density of non-spherical particles as derived from combined measurements of aerodynamic and mobility equivalent size, J. Aerosol Sci., 38, 431-443, doi: 10.1016/j.jaerosci.2007.01.002, 2007.

Schnaiter, M., Linke, C., Mohler, O., Naumann, K. H., Saathoff, H., Wagner, R., Schurath, U., and Wehner, B.: Absorption amplification of black carbon internally mixed with secondary organic aerosol, J. Geophys. Res.-Atmos., 110, doi: 10.1029/2005jd006046, 2005.

Silva, P. J., Liu, D. Y., Noble, C. A., and Prather, K. A.: Size and chemical characterization of individual particles resulting from biomass burning of local Southern California species, Environ. Sci. Technol., 33, 3068-3076, doi: 10.1021/es980544p, 1999.

Song, X. H., Hopke, P. K., Fergenson, D. P., and Prather, K. A.: Classification of single particles analyzed by ATOFMS using an artificial neural network, ART-2A, Anal. Chem., 71, 860-865, doi: 10.1021/ac9809682, 1999.

Spencer, M. T., Shields, L. G., and Prather, K. A.: Simultaneous measurement of the effective density and chemical composition of ambient aerosol particles, Environ. Sci. Technol., 41, 1303-1309, doi: 10.1021/es061425+, 2007.

Tajima, N., Fukushima, N., Ehara, K., and Sakurai, H.: Mass range and optimized operation of the aerosol particle mass analyzer, Aerosol Sci. Technol., 45, 196-214, doi: 10.1080/02786826.2010.530625, 2011.

Turpin, B. J., and Lim, H.-J.: Species contributions to PM2.5 mass concentrations: revisiting common assumptions for estimating organic mass, Aerosol Sci. Technol., 35, 602-610, doi: 10.1080/02786820119445, 2001.

Wentzel, M., Gorzawski, H., Naumann, K. H., Saathoff, H., and Weinbruch, S.: Transmission electron microscopical and aerosol dynamical characterization of soot aerosols, J. Aerosol Sci., 34, 1347-1370, doi: 10.1016/s0021-8502(03)00360-4, 2003.

Zauscher, M. D., Wang, Y., Moore, M. J. K., Gaston, C. J., and Prather, K. A.: Air Quality Impact and Physicochemical Aging of Biomass Burning Aerosols during the 2007 San Diego Wildfires, Environ. Sci. Technol., 47, 7633-7643, doi: 10.1021/es4004137, 2013.

Zhai, J., Wang, X., Li, J., Xu, T., Chen, H., Yang, X., and Chen, J.: Thermal desorption single particle mass spectrometry of ambient aerosol in Shanghai, Atmos. Environ., 123, 407-414, doi: 10.1016/j.atmosenv.2015.09.001, 2015.

Zhang, R., Khalizov, A. F., Pagels, J., Zhang, D., Xue, H., and McMurry, P. H.: Variability in morphology, hygroscopicity, and optical properties of soot aerosols during atmospheric processing, P. Natl. Acad. Sci. USA, 105, 10291-10296, doi: 10.1073/pnas.0804860105, 2008.

835

836
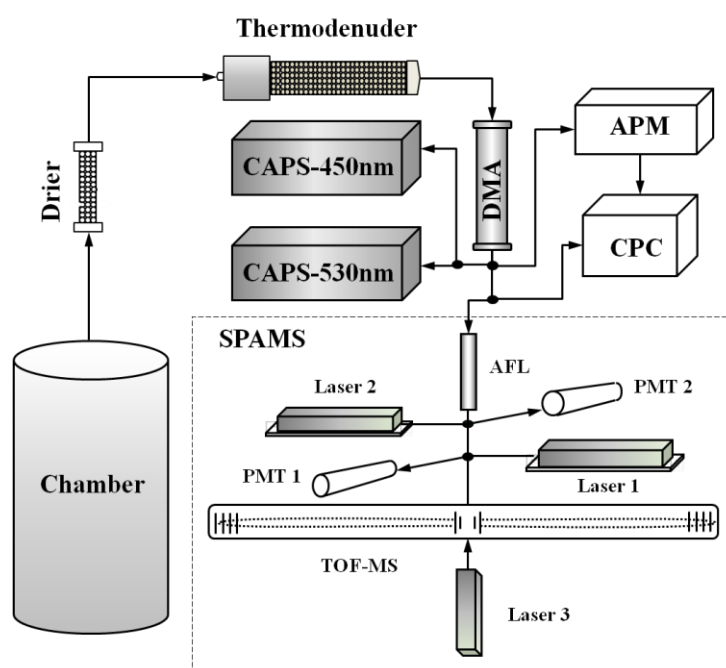
Figure 1. Schematic of the instrumental setup. The CAPS, DMA, CPC, APM and
SPAMS represent Cavity Attenuated Phase Shift spectroscopy, Differential Mobility
Analyzer, Condensation Particle Counter, Aerosol Particle Mass analyzer and Single
Particle Aerosol Mass Spectrometer, respectively.

841

842
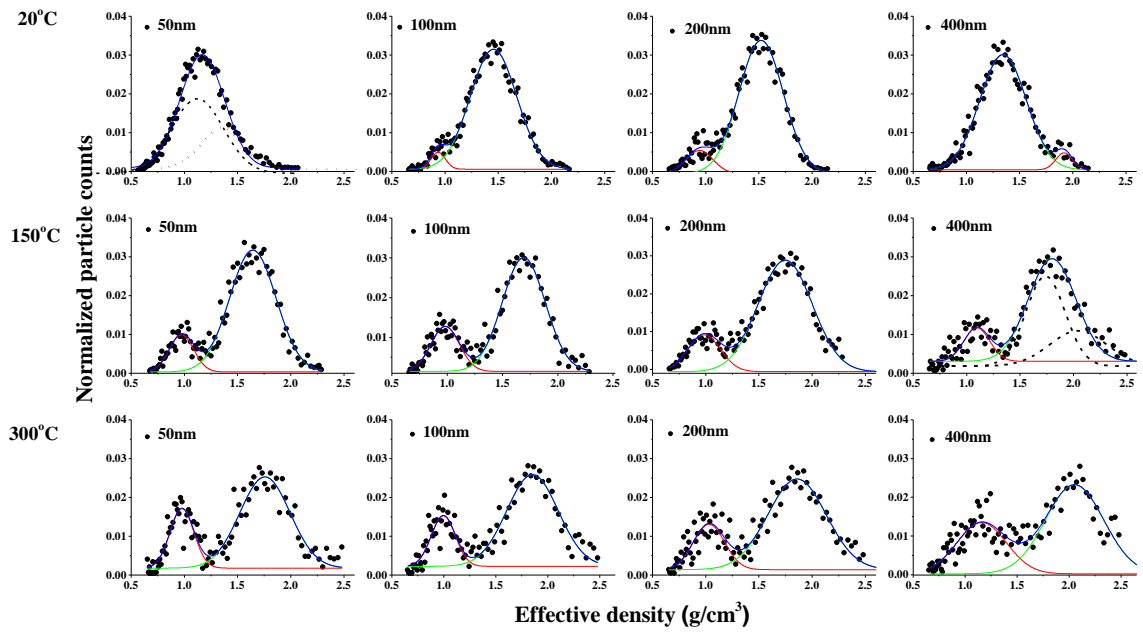
Figure 2. Average density distributions of 50, 100, 200, and 400 nm particles selected
by DMA at 20 °C (room temperature), 150 °C, and 300 °C. Gaussian model was
applied in fitting each density scan (red and green lines). Black dashes were the
assumption Gaussian models application.

847
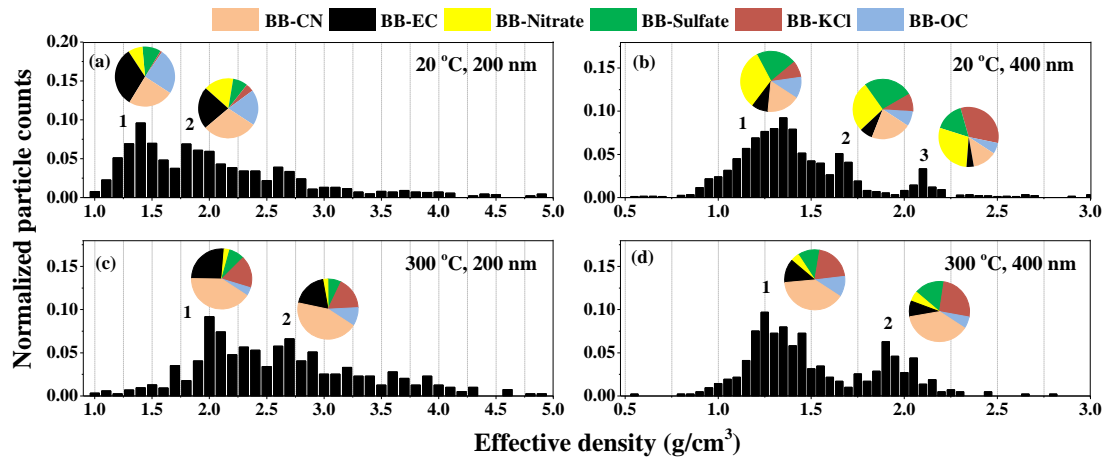
848

849 Figure 3. Vacuum aerodynamic size distributions detected by the SPAMS of 200 nm

850 and 400 nm electrical mobility size-selected biomass burning particles and pie charts

851 for the particle types in different aerodynamic modes at 20 °C (room temperature) and

852 300 °C.

853
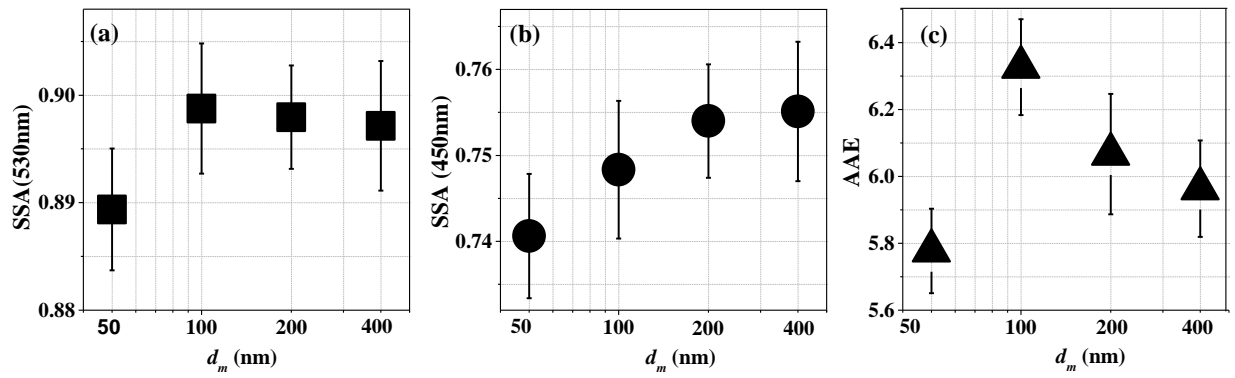
854

855 Figure 4. (a)-(b): Size-resolved single scattering albedo (SSA) at wavelengths of 530

856 nm and 450 nm. (c): Ångström absorption exponent (AAE) of biomass burning

857 particles at room temperature (20°C).

858